Influence of the X-point location on the edge plasma transport in the J-TEXT tokamak with a high-field-side single-null divertor

Hao WANG (王灏)[1], Yunfeng LIANG (梁云峰)[1,2,3,*], Shuai XU (徐帅)[2,*], Zhonghe JIANG (江中和)[1], Yuhe FENG (冯玉和)[4], A. KNIEPS[2], P. DREWS[2], Jie YANG (阳杰)[1], Xin XU (徐鑫)[1], Ting LONG (龙婷)[5], Shaodong JIAO (焦少东)[1], Xiaolong ZHANG (张晓龙)[6], Zhigang HAO (郝志刚)[1], Qinglong YANG (杨庆龙)[1], Zhipeng CHEN (陈志鹏)[1], Zhongyong CHEN (陈忠勇)[1], Nengchao WANG (王能超)[1], Zhoujun YANG (杨州军)[1], Xiaoqing ZHANG (张晓卿)[1], Yonghua DING (丁永华)[1], Yuan PAN (潘垣)[1] and the J-TEXT Team[1,a]

[1]International Joint Research Laboratory of Magnetic Confinement Fusion and Plasma Physics, State Key Laboratory of Advanced Electromagnetic Engineering and Technology, School of Electrical and Electronic Engineering, Huazhong University of Science and Technology, Wuhan 430074, People's Republic of China

[2]Forschungszentrum Jülich GmbH, Institut für Energie- und Klimaforschung-Plasmaphysik, Partner of the Trilateral Euregio Cluster (TEC), 52425 Jülich, Germany

[3]Institute of Plasma Physics, Chinese Academy of Sciences, Hefei 230031, People's Republic of China

[4]Max-Planck-Institutfur Plasma physik, EURATOM Association, 17491 Greifswald, Germany

[5]Southwestern Institute of Physics, Chengdu 610041, People's Republic of China

[6]Advanced Energy Research Center, Shenzhen University, Shenzhen 518060, People's Republic of China

*E-mails of corresponding authors: y.liang@fz-juelich.de, s.xu@fz-juelich.de

Abstract

The high-density experiments in the high field side (HFS) mid-plane single-null divertor configuration have been performed for the first time on J-TEXT. The experiments show an

---

[a] See the author list of "Liang Y. et al 2019 Overview of the recent experimental research on the J-TEXT Tokamak, Nucl. Fusion 59 112016"

increase in the highest central-channel line-averaged density from $2.73 \times 10^{19}\ \mathrm{m}^{-3}$ to $6.49 \times 10^{19}\ \mathrm{m}^{-3}$ while the X-point moves away from the target by increasing the divertor coil current. The corresponding Greenwald fraction rises from 0.50 to 0.79. For the impurity transport, the density normalized radiation intensity (AXUV and SXR) of the central channel density decreased significantly (> 50%) with an increase in the plasma density. To better understand the underlying physics mechanisms, the 3D edge Monte Carlo code coupled with EIRENE (EMC3-EIRENE) has been implemented for the first time on J-TEXT. The simulation results show a good agreement with the experimental findings. As the X-point moves away from the target, the divertor power decay length drops and the SOL impurity screening effect is enhanced.

Keywords: divertor configuration, EMC3-EIRENE, edge plasma transport

1. Introduction

Compared to the limiter configuration, the divertor configuration has advantages in manipulating the power flow, controlling the impurity production, and removing reaction waste[1–5]. ITER will operate in a divertor configuration [6]. The method discussed here to reduce the target heat load is to optimize the downstream flux [7–10] because the particle temperature and density at the SOL upstream are mainly related to the core plasma, depending on the conditions of the fusion reaction. The SOL transport not only influences the plasma-wall interaction, but also affects the core confinement. Besides, the impurity generation and the impurity transport such as impurity screening are also affected by the edge plasma transport. Therefore, it is essential to understand the SOL plasma transport for optimized divertor operation.

J-TEXT is a conventional iron core tokamak with a divertor power system, which supplies 400 V/25 kA bipolar direct current for 500 ms [11]. It has reached an advanced level in the study of magnetic perturbation physics and plasma disruption mitigation, but the absence of a divertor configuration research hinders further explorations [12]. A divertor configuration on J-TEXT may contribute to the improvement of operation parameters and an expansion of its physics research scope. Additionally, the application of a divertor configuration on J-TEXT would offset the gap between itself and advanced devices. Therefore these experiments at J-TEXT will have a greater degree of universality.

Recently, a series of high density experiments in high-field side (HFS) mid-plane single-null divertor configuration was carried out for the first time on J-TEXT [13]. These experiments show that the divertor configuration improves the density limit, and that the edge plasma transport is affected by the distance between the X-point and the HFS target. The diagnostic results obtained from the experiments are the foundation to understand the physical mechanism of this divertor configuration. To qualitatively describe the transport processes, especially at the plasma edge, the three-dimensional numerical simulation code EMC3-EIRENE [14–20] was applied for the first time on J-TEXT. The main reason for applying the EMC3-EIRENE code to the current axisymmetric divertor configuration of J-TEXT is to experimentally validate the 3D code before it is used to real 3D divertor configurations caused by RMP-fields planned in the near future.

In this HFS mid-plane single-null divertor configuration on J-TEXT, the X-point is located in the favorable curvature area. This research is dedicated to the understanding of the factors influencing the edge plasma- and impurity-transport, such as the X-point location and the density ramp-up. Additionally, the possibility of entering the high recycling has been studied.

This paper is structured as follows. In section 2, the experimental results are presented, including the experimental setup (section 2.1) and the diagnostic measurement analysis (2.2). In section 3, the comparison between simulations and experiments is presented and discussed in detail. Finally, the conclusions are summarized and discussed in section 4.

2. High-density experiments with different divertor coil currents

2.1. Experiment setup

J-TEXT is a circular medium-sized tokamak with a major radius R_0 = 1.05 m, which can be operated in limiter and the HFS divertor configuration. The first physical experiment in HFS divertor configurations is analyzed and discussed in this work. The HFS target located at R_{target} = 75.4 cm is made of graphite and covered with SiC film. The wall conditioning is realized by the glow discharge. In this work, J-TEXT was operated in the HFS mid-plane single-null divertor configuration with a toroidal magnetic field of B_{t} = 2 T at the magnetic axis. The plasma current I_{p} = 150 kA was fixed through all experiments with only Ohmic heating of $P_{\mathrm{ohmic}} \approx 270$ kW.

The X-point location was controlled by changing the divertor coil current with a ramp-up time of $\sim$150 ms. The density ramp-up was realized by gas puffing from the lower window of the port 8 at $R = 105$ cm, $Z = -32.6$ cm. The divertor current I_{div} was set as 15 kA, 12 kA, 10 kA and 8 kA, respectively. The radial distributions of the plasma electron temperature T_{e} and the density n_{e} were measured by a reciprocating probe (RP) system installed on the upper window of port 12 at R = 105 cm. The probe was stopped at $Z = 20$ cm to measure the time evolution of the ion saturation current, and the measured results were compared with the ion saturation current of the downstream target probe to observe the upstream and downstream changes. The line-integrated density was derived from the multi-channel polarimeter interferometer system (POLARIS). The soft X-ray diagnostic (SXR), the absolute extreme ultraviolet diagnostic (AXUV), the carbon III (CIII) photodiode array (PDA), the Doppler coherence imaging spectroscopy interferometer (CIS) provided the radiation signals to investigate the evolution of the impurity density and the CIII radiation distribution with increasing plasma density [21–24]. Figure 1 shows the optical path distributions of the above diagnostic systems. The toroidal angle of the optical diagnostic is limited by an optical channel slit. The toroidal width of the slit is 5 mm, 4.4 mm and 33 mm corresponding to AXUV, SXR and CIII PDA. Because of the small optical channel slit, the optical path distributions are regarded as 2D in the experiment. Besides, the divertor configuration is toroidal symmetry in this paper.

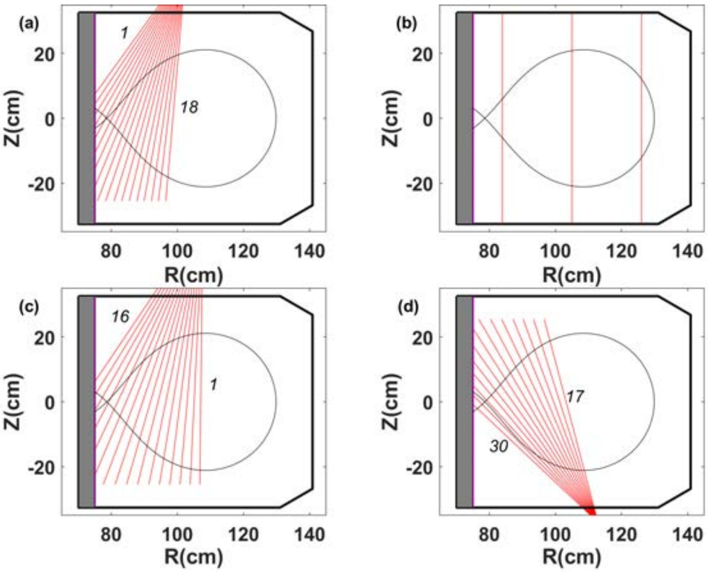

Figure 1. Optical path distributions of (a) CIII, (b) POLARIS, (c) AXUV, (d) SXR. The *R*, *Z* locations of the AXUV focus, CIII focus, SXR focus are (107.7 cm, 55.6 cm), (102.6 cm, 46.2 cm), (112.9 cm, −31.2 cm).

2.2. The influence of X-point and the density ramp-up on the edge plasma transport

For better understanding the influence of the X-point location and the plasma density on the edge plasma transport, a series of experiments has been performed on J-TEXT. An overview of the key discharges is shown in figure 2. The X-point location (distance between the X-point and the high-field side target) influences the maximum density reachable before disruption. As seen in figure 2, with continuous gas puffing, the chord integral density of the central channel measured by POLARIS gradually increases over time. The maximum integrated density before disruption increases with increasing I_{div}. The detailed data are shown in table 1. Figure 3 indicates the separatrix locations reconstructed by the EFIT [25] code. It should be mentioned that the plasma in the case of $I_{\mathrm{div}} = 8\ \mathrm{kA}$ operates in a limiter configuration due to the X-point being located behind the target, which is represented by the negative corresponding Δr in table 2. This explains why the maximum chord integral density drops considerably with $I_{\mathrm{div}} = 8\ \mathrm{kA}$. Combined with the EFIT results, the line average density and Greenwald fraction [26] are obtained as shown in table 2. The divertor configuration improves the density limit compared to the limiter configuration, increasing the Greenwald fraction from 0.50 to 0.79.

The plasma density and the X-point location also influence the edge impurity transport. The radiation intensity measured by AXUV, SXR, and CIII rises with increasing plasma density. In table 1, the density normalization ratio of I_{AXUV} before disruption to I_{AXUV} at 200 ms is less than 50% in the cases of $I_{\mathrm{div}} = 15\ \mathrm{kA}, 12\ \mathrm{kA}$. The density normalization radiation intensity decreases significantly while the temperature changes little. This proves that the X-point moving away from the target helps in reducing the core impurity concentration. Figure 4 shows the time evolution of

the radiation intensity in the studied experiments. When comparing the radiation intensities measured by AXUV and SXR at different I_{div}, one finds that the impurity radiation in both the core and the SOL is reduced when the X-point moves away from the target. This observation supports the hypothesis that moving the X-point away from the target can improve the SOL impurity screening effect, thus reducing the impurity concentration in the core plasma in J-TEXT.

Table 1. Central channel diagnostic results.

I_{div} (kA)	$n_{\text{e}}L$ (10^{19} m^{-2})		I_{AXUV} (a.u.)			I_{SXR} (a.u.)		
	200 (ms)	Before disruption	200 (ms)	Before disruption	Density normalization ratio	200 (ms)	Before disruption	Density normalization ratio
15	1.22	2.72	0.338	0.542	0.32	0.319	0.602	0.37
12	1.07	2.62	0.308	0.729	0.39	0.342	0.965	0.47
10	1.51	2.57	0.413	0.742	0.62	0.479	1.178	0.84
8	0.84	1.29	0.499	0.766	0.65	0.671	1.298	0.82

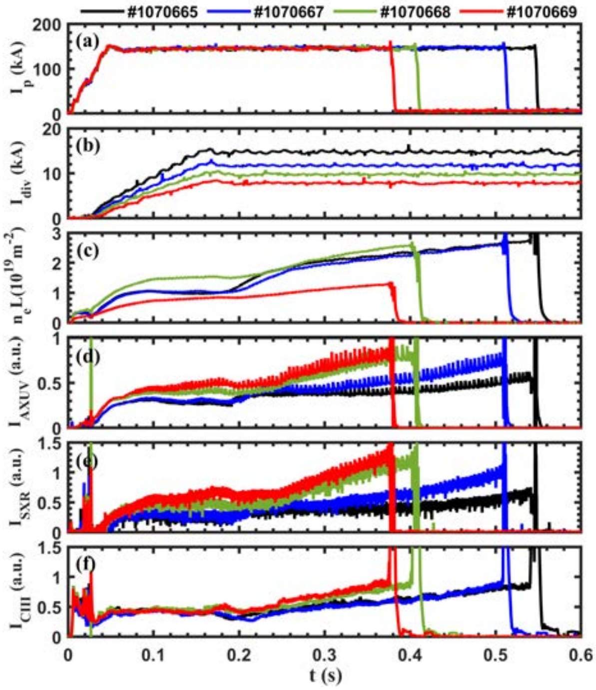

Figure 2. (a) Plasma current, (b) divertor coil current, (c) central channel integral density, (d) AXUV central channel radiation intensity, (e) SXR central channel radiation intensity, (f) CIII innermost channel radiation intensity. (Divertor coil currents in the shot 1070665, 1070667, 1070668, 1070669 are 15 kA, 12 kA, 10 kA, 8 kA, respectively.)

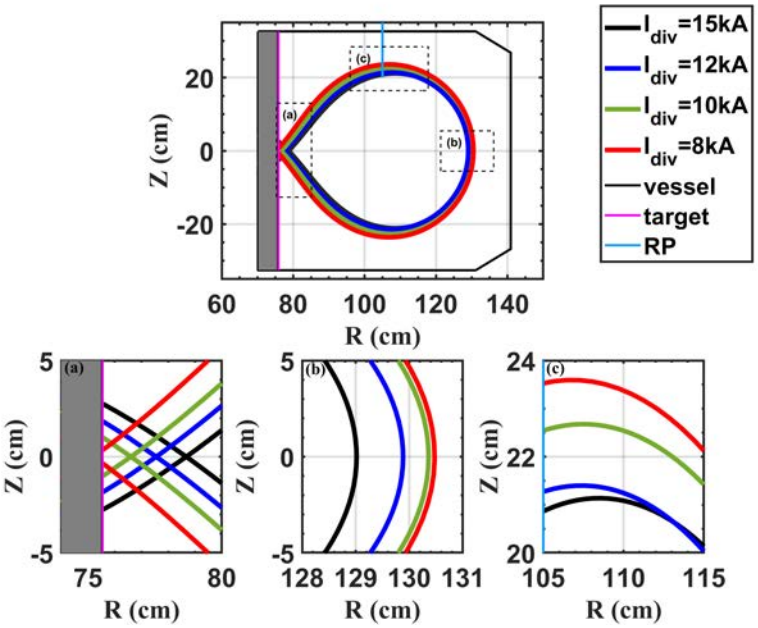

Figure 3. Separatrix generated from EFIT. (a), (b), (c) corresponds to the area of the above full picture.

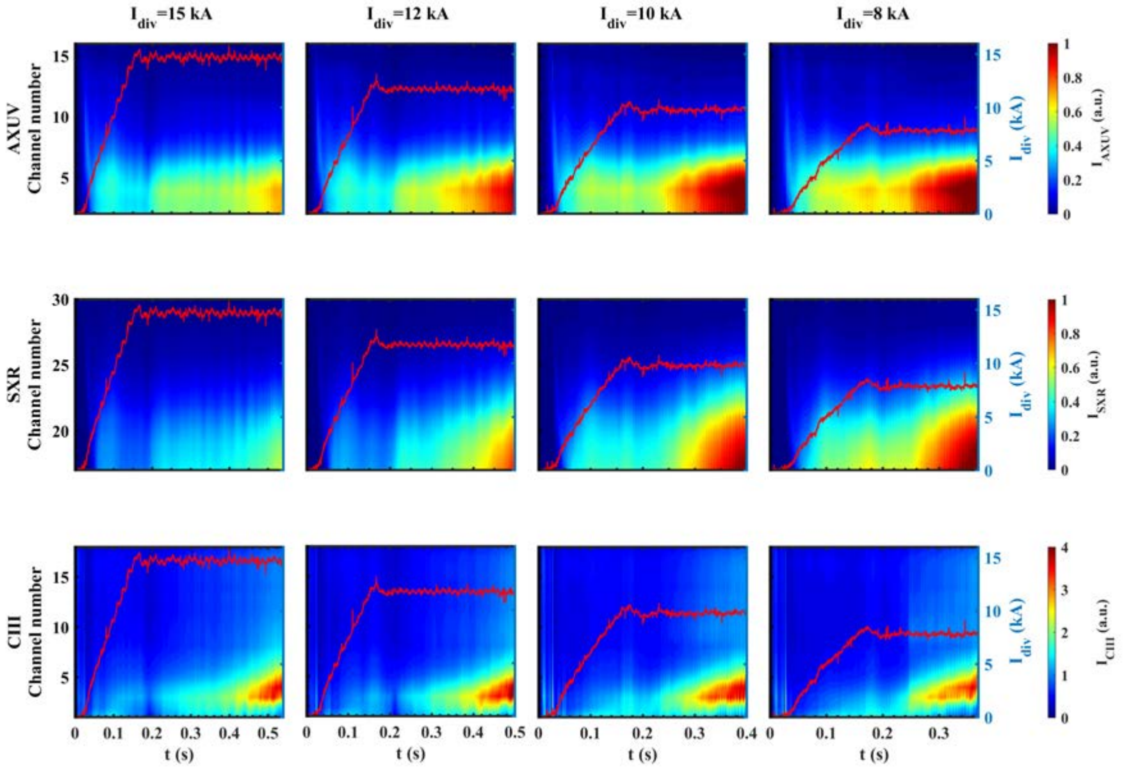

Figure 4. The evolution of the radiation intensity measured by AXUV, SXR, CIII PDA. The line in each contour map represents the divertor coil current. The divertor coil currents corresponding to each column are 15 kA, 12 kA, 10 kA, 8 kA, respectively.

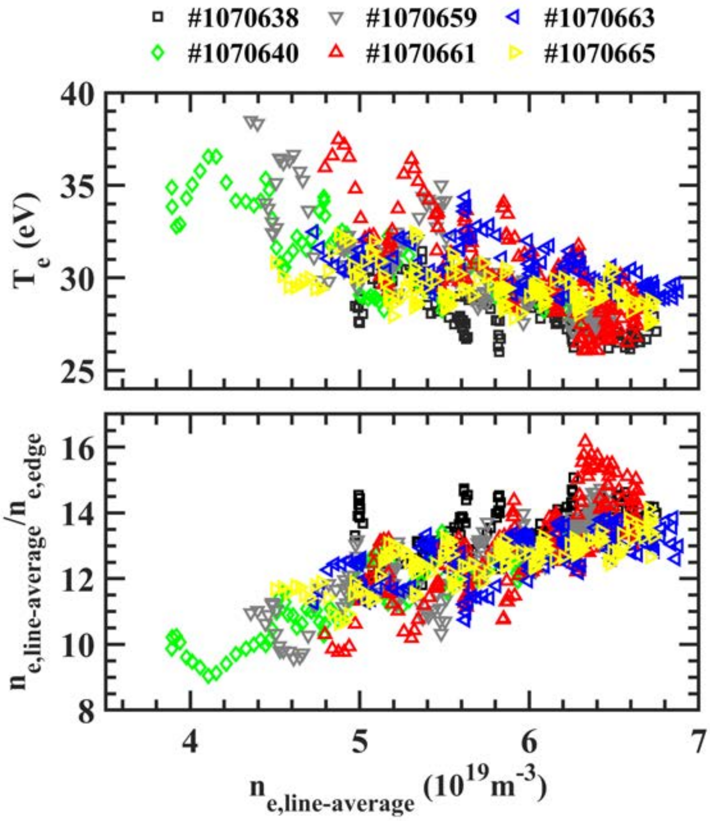

Figure 5. The edge electron temperature T_e and the ratio of the central channel line-average electron density to the edge electron density $n_\mathrm{e,line-average}/n_\mathrm{e,edge}$ are as function of the central channel line-average electron density $n_\mathrm{e,line-average}$. ($I_\mathrm{div} = 15\ \mathrm{kA}$ at all the shots. The *Z* location of probe is 20 cm, near the separatrix.)

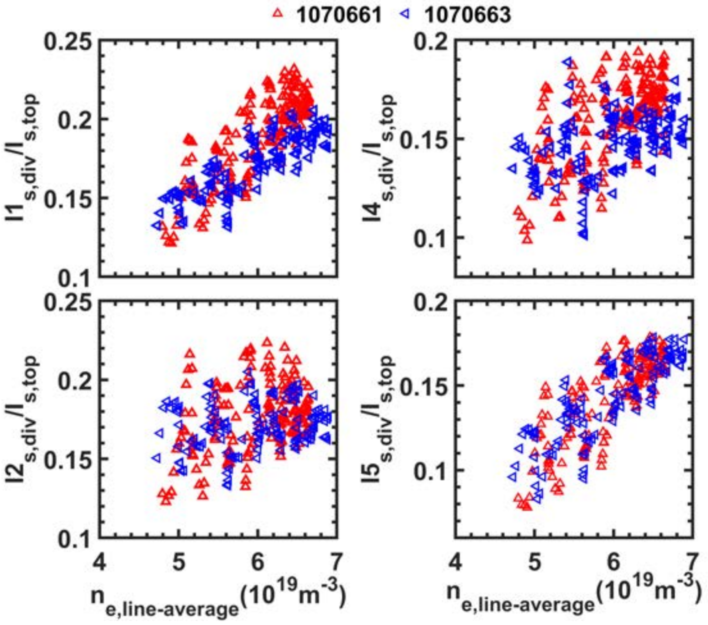

Figure 6. The ratio of target ion saturation flux to ion saturation flux measured by the RP is as a function of central channel line-average electron density $n_\mathrm{e,line-average}$ (I_div=15 kA). The *Z* locations of target probe corresponding to I1, I2, I4, I5 are 7.6 cm, 3.8 cm, −3.8 cm, −7.6 cm.

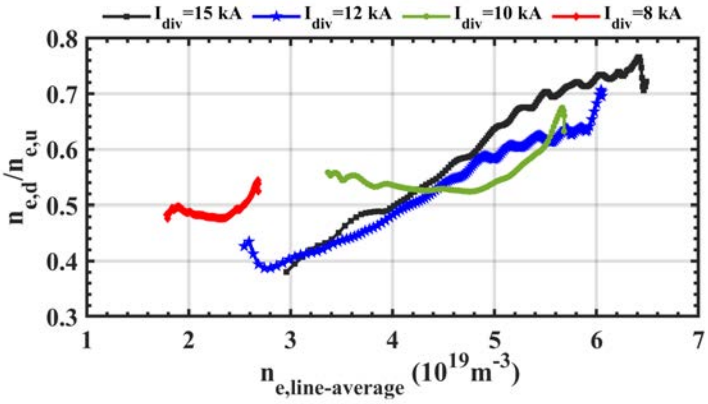

Figure 7. The ratio of downstream electron density to upstream electron density is as a function of the central channel line-average electron density $n_{\mathrm{e,line-average}}$, in the case of I_{div} =15 kA, 12 kA, 10 kA, 8 kA. As shown in figure 1, the line-average density is measured by POLARIS at R=105 cm. The upstream electron density is measured by POLARIS at R=126 cm, and the downstream electron density is measured by POLARIS at R=84 cm.

Table 2. Location of the X-point and the corresponding density-related parameters ($\Delta r = R_{\mathrm{X-point}} - R_{\mathrm{target}}$).

I_{div} (kA)	Δr (cm)	$\bar{n}_{\mathrm{e}}$ (10^{19} m^{-3})	$n_{\mathrm{Greenwald}}$ (10^{19} m^{-3})	Greenwald fraction
15	3.27	6.49	8.21	0.79
12	2.15	5.77	7.53	0.77
10	1.21	5.66	7.28	0.78
8	-0.20	2.73	5.49	0.50

During the density ramp-up, the SOL electron temperature dropped and the core electron density rose faster than the SOL electron density, just as the downstream ion saturation flux increased faster than the ion saturation flux measured by the reciprocating probe. In the shot with $I_{\mathrm{div}} = 15$ kA, the reciprocating probe was fixed at Z=20 cm in order to measure the time evolution of the SOL upstream electron density and temperature. Diagnostic results indicate that the probe had not yet reached the separatrix, while the EFIT reconstructions suggest the opposite. The discrepancy between diagnostic results and EFIT reconstructions is caused by a displacement of the central current and the resulting profile deformation. This also explains the presence of large fluctuations in the measurements. Repeated measurements observe a trend in the SOL, with electron temperature dropping by about 25% and the $n_{\mathrm{e,line-average}}/n_{\mathrm{e,edge}}$ increasing by about 40% with increasing line average density (covering a roughly 70% increase). These observations are shown in figure 5. As visible in figure 6, the ratio of the target ion saturation current to the ion saturation current measured by the RP increases with increasing density, while the ratio of the HFS integration density to low field side integration density shows the same trend in figure 7. For the carbon impurity, figure 8 shows that the CIII radiation is concentrated in the X-point area, and with the X-point moving towards the target, the CIII radiation concentration area moves deeper towards the core during the density ramp-up.

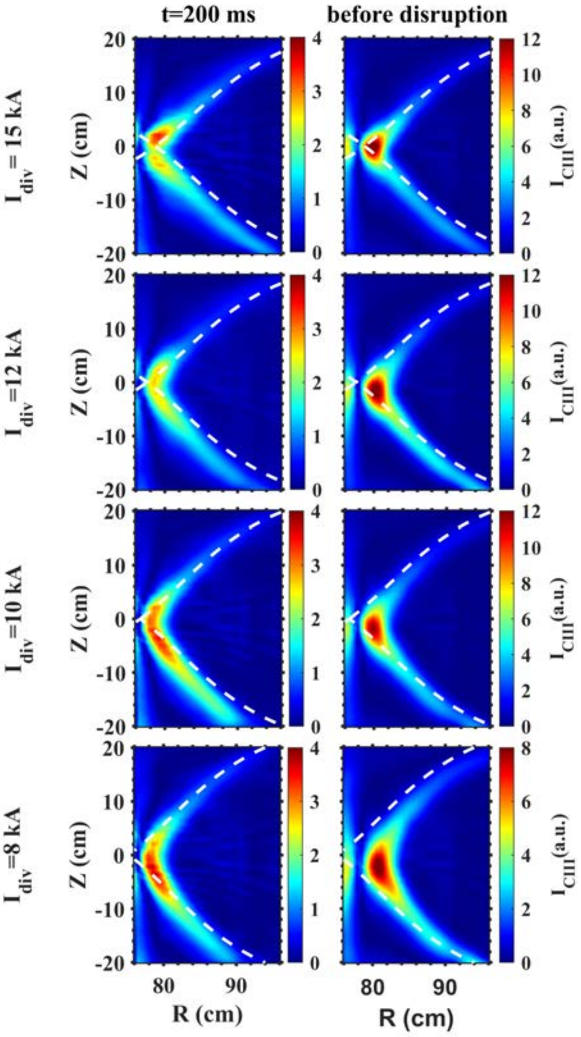

Figure 8. The 2D CIII radiation intensity distribution reconstructed from the Doppler CIS diagnostics. The line in each map represents the position of the separatrix.

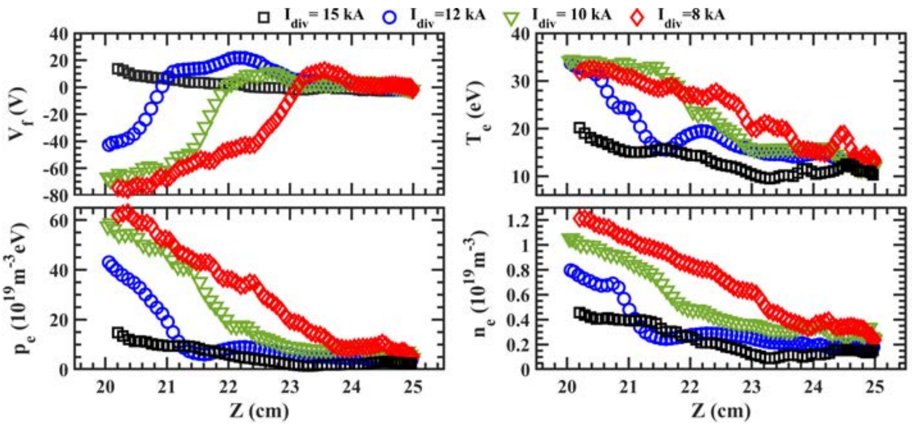

Figure 9. The radial distributions of the floating potential V_f, the electron temperature T_e, the electron density n_e, the pressure p_e measured by the reciprocating probe system with different I_div.

The distribution of the edge plasma depends on the distance between the X-point and the target, implying that it is indeed affected by the different HFS mid-plane single-null divertor configurations. In the core area, the gradient of the electron density distribution is larger than that in the SOL. Meanwhile, the gradient near the separatrix increases with an increase in I_div. However, the gradient tends to be the same in the deeper core area. This reflects the influence of the X-point location on the edge plasma transport.

3. Simulation procedure & results

In order to better understand the observed effects, edge plasma transport simulations were performed with the EMC3-EIRENE code. EMC3-EIRENE is a powerful code to simulate the edge plasma transport with low impurity concentrations. EMC3-EIRENE consists of the 3D edge fluid transport code EMC3, which solves the Braginskii's fluid equations, and the 3D kinetic neutral particle transport code EIRENE, which solves the kinetic Boltzmann equations. The EMC3 code applies an advanced Monte-Carlo algorithm to solve the fluid equations. The code has been widely used in multiple devices including stellarators and tokamaks, such as W7-X [27], LHD

[28–32], TEXTOR-DED [33], DIII-D [34], ASDEX-U [35], JET [36], TCV [37], EAST [38–44]. In this work, the grid generator of EMC3-EIRENE is adapted to the J-TEXT axisymmetric HFS divertor configurations. The 3D code can reproduce the experimental results and provide more detailed information on SOL plasma, such as the plasma density, the plasma temperature and the impurity density, as well as the divertor particle flux and the divertor heat flux.

3.1. Generation of the simulation grid

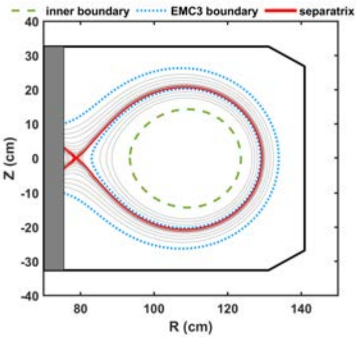

Figure 10. The computational grid at $\varphi = 0^{\circ}$, generated based on the EFIT code for shot 1070665 at 420 ms.

The 2D equilibrium is provided by EFIT. The 3D grid generation procedure starts with the construction of a 2D grid in an arbitrary toroidal plane due to the axisymmetry of the divertor configuration. The generation of the 2D grid requires to first find the X-point and O-point, and then to find the magnetic flux surfaces according to the given poloidal and radial resolution. As shown in figure 10, the 2D grid consists of three distinct regions, namely the core, the SOL, and the private flux region (PFR). Adjacent sub-domains have to share common grid points on their interface to ensure that all sub domains can form the whole real space, so the number of the poloidal grid points in different regions has to satisfy the constraint $n_{\mathrm{p,SOL}} = n_{\mathrm{p,core}} + n_{\mathrm{p,PFR}}$. The 3D mesh is generated by tracing magnetic field lines from the 2D grid points over a finite phi-angle. For the axisymmetric case addressed in this paper, the choice of the toroidal domain length can be arbitrary. In realistic 3D configurations, it usually spans one field period by tracing magnetic field lines. The grids are constructed for Ohmic shots 1070665 at 420 ms, 1070667 at 400 ms and 1070668 at 350 ms, corresponding to I_{div} = 15 kA, 12 kA, 10 kA, respectively.

3.2. Reconstruction of J-TEXT divertor plasmas in EMC3-EIRENE

In order to reconstruct the J-TEXT divertor plasmas with I_{div} = 15 kA, 12 kA, 10 kA, the main input parameters for EMC3-EIRENE need to be determined experimentally first, including the separatrix electron density $n_{\mathrm{e,sep}}$, the particle cross field transport coefficients of main plasma and impurity $D_{\perp}$, $D_{\perp,\mathrm{imp}}$, the energy cross field transport coefficients of electrons and ions $\chi_{\perp,\mathrm{e}}$, $\chi_{\perp,\mathrm{i}}$, the power entering SOL P_{SOL} and the impurity sputtering coefficient. The separatrix electron density, the cross-field diffusivity of the background plasma and the anomalous conductivity of electrons are mainly determined by fitting the electron density and temperature radial distribution measured by the RP, while also considering the measurements from Doppler CIS and radiation diagnostics.

Then, that $D_{\perp}$ = $D_{\perp,\mathrm{imp}}$, $\chi_{\perp,\mathrm{e}}$ = $\chi_{\perp,\mathrm{i}}$ are presumed. The inner boundary is set to the normalized magnetic flux surface 0.6. The P_{SOL} is set equally between electrons and ions in EMC3-EIRENE input parameters. The boundary condition applied at the divertor targets is Bohm condition. The impurity source flux equals the impurity sputtering coefficient times the recycling flux. The simulation is based on the ADAS [45] database.The current diagnostic capability on J-TEXT does not allow for quantification of the existing impurity species and the associated radiation, especially in the core, which makes the estimation of P_{SOL} difficult. For this reason, in the simulation, P_{SOL} was scanned in a step of 13.5 kW, which is 5% of the total Ohmic heating power of 270 kW. Given the low T_{e} values measured by the RP in the SOL (see figure 9), both the chemical sputtering and physical sputtering processes on the graphite target are covered by assuming an effective sputtering coefficient of 0.04 [38, 46, 47]. The actual location of the separatrix is corrected by assuming that the RP measures a change of floating potential from positive to negative at the SOL-core interface. According to this correction, the measured profiles at I_{div}=15 kA, 12 kA, 10 kA have been shifted by 0.534 cm, 0.358 cm, 0.623 cm in Z coordinate direction, respectively. Effective-Z effects are not considered in either the evaluation of the RP results or in the simulations. Under this assumption, together with the separatrix shifts, the main code input parameters are determined, as listed in table 3, which result in best matches with the RP profiles.

Table 3. Simulation parameters.

I_{div} (kA)	$n_{\mathrm{e,sep}}$ (10^{18} m^{-3})	$D_{\perp}$ ($\mathrm{m}^2\mathrm{s}^{-1}$)	$\chi_{\perp}$ ($\mathrm{m}^2\mathrm{s}^{-1}$)	P_{SOL} (kW)	$D_{\perp,\mathrm{imp}}$ ($\mathrm{m}^2\mathrm{s}^{-1}$)	Sputtering coefficient
15	5.5	1	4	67.5	1	0.04
12	7	1	4	108	1	0.04
10	9	1	4	121.5	1	0.04

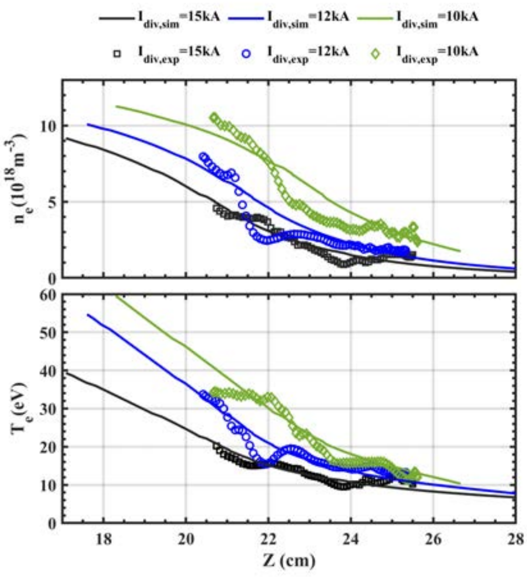

Figure 11. Radial distributions of electron temperature and density simulated by EMC3-Eirene in comparison with those measured by the RP when the RP processes from 264 ms to 330 ms.

The simulated radial distributions are mostly consistent with the RP results as shown in figure 11. The discrepancies between the simulations and the RP measurements may result from the displacement of the plasma current center, the density increase when the RP processes or other possibilities. Figure 12 shows the resulting 2D distributions of the electron density, the electron temperature, the ion temperature and the Mach number with I_{div} = 15 kA, 12 kA, 10 kA. The results are upper and lower symmetry.

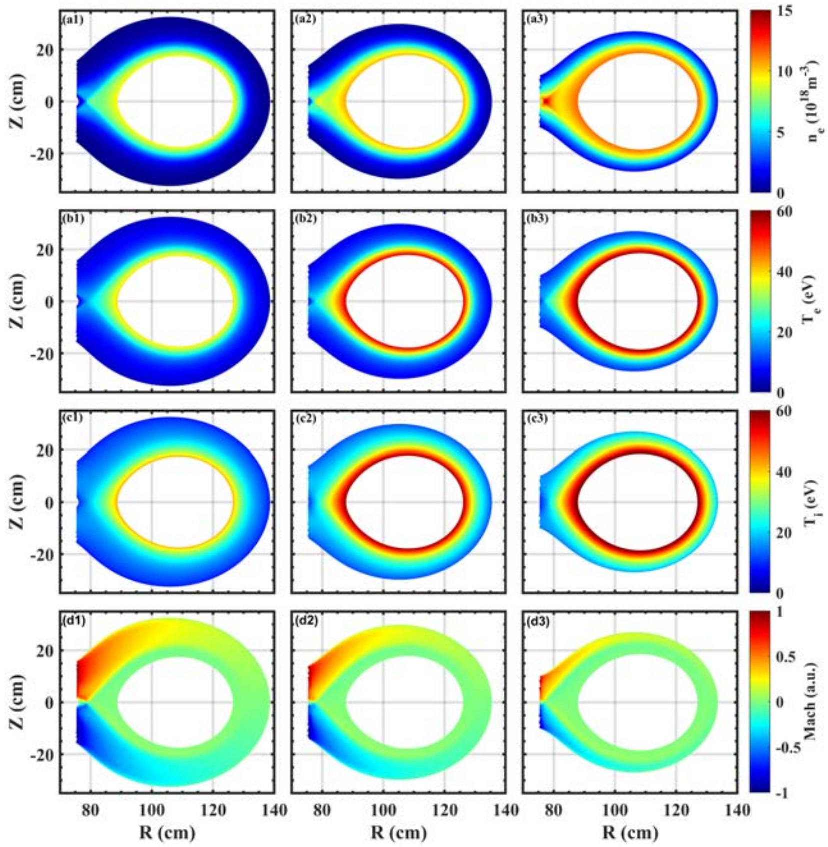

Figure 12. 2D distributions of edge plasma parameters from the EMC3-EIRENE simulations for three different divertor coil currents. (1) 15 kA (left column), (2) 12 kA (middle column), and (3) 10 kA (right column).

Even though the simulation results are consistent with the RP diagnostic results in the upstream region, there is a discrepancy in CIII location between the simulation results and the Doppler CIS diagnostic results. As shown in figure 13 , the CIII impurity concentrates near the strike point, while the Doppler CIS diagnostic results show that the CIII impurity concentrates near the X-point.

This indicates that the temperature at the X-point area in the simulation is higher than that in the experiment implying that the actual P_{SOL} is lower than assumed in the simulation. To confirm this point, P_{SOL} is gradually reduced in the simulation. Using the I_{div}=15 kA case as an example, Figure 14 shows how the CIII-radiation distribution develops as P_{SOL} is decreased from 67.5 kW to 54 kW and further to 40.5 kW. In the lowest P_{SOL} case, a second peak of CIII-radiation occurs near the X-point just inside the LCFS, as also indicated by CIII-radiation from the CIS measurements shown in figure 8. Similar simulations with reduced P_{SOL} were also performed for the cases of $I_{\mathrm{div}} = 12\,\mathrm{kA}$ and 10 kA. The results are displayed in figure 15, which are qualitatively

consistent with the experimental findings in figure 8. Therefore, in general, reducing P_{SOL} increases the CIII radiation around the X-point. However, the simulated electron temperature radial distribution drops at the same time, resulting in a discrepancy between the modelling and the RP data. The simulations cannot get good agreement with the above two diagnostic data at the same time, possibly due to the underestimate of the impurity cross-field coefficient or the underestimate of the impurity sputtering initial energy. The scanning of impurity cross-field coefficient $D_{\perp,\mathrm{imp}}$ and the impurity sputtering initial energy $E_{0,\mathrm{imp}}$ has been carried out. As shown in figure 16 and figure 17, the increase in the two parameters results in the increase in CIII radiation at the X-point. However, the CIII radiation is still intense near the strike point. Another possiblity is the existence of the other impurities such as oxygen, nitrogen detected by the residual gas analysis in the vacuum condition of J-TEXT [48]. Oxygen radiation should also be located in the edge region of the plasma, and its effects cannot be approached well by reducing the P_{SOL}.

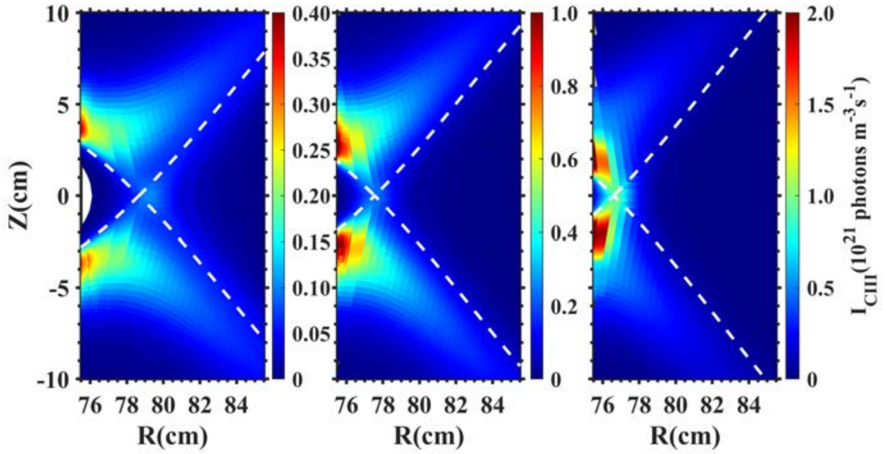

Figure 13. 2D CIII radiation intensity distributions with $I_{\mathrm{div}} = 15$ kA, 12 kA, 10 kA, respectively. The dash lines represent the locations of the separatrix.

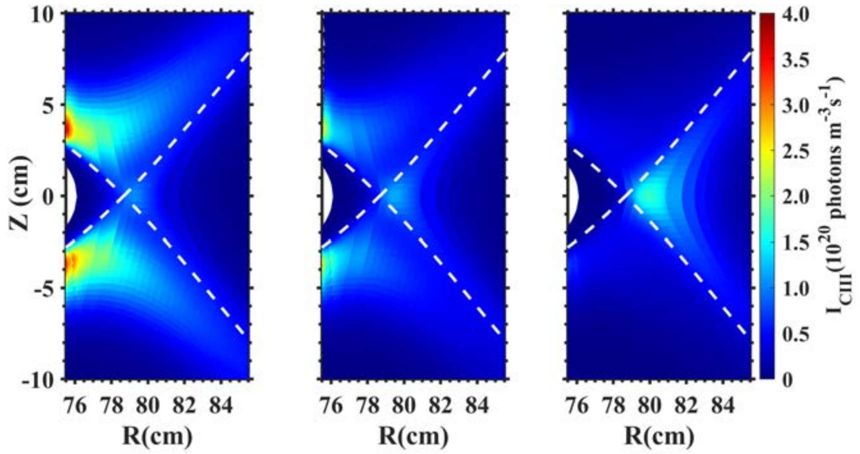

Figure 14. 2D CIII radiation intensity distributions for $P_{\mathrm{SOL}} = 67.5$ kW, 54 kW, 40.5 kW with $I_{\mathrm{div}} = 15$ kA. The dashed lines represent the locations of the separatrix.

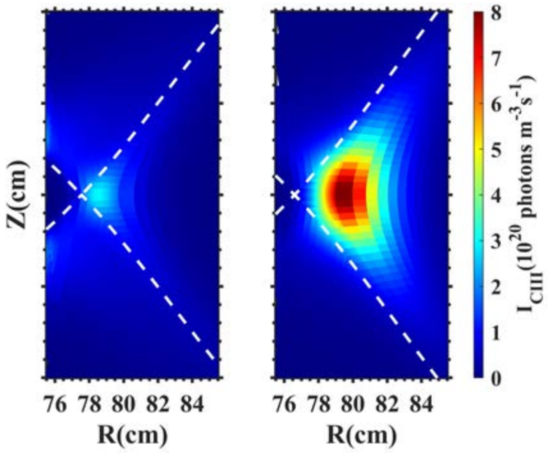

Figure 15. The 2D CIII radiation intensity distributions with lower P_{SOL} for $I_{\mathrm{div}} = 12$ kA, 10 kA correspondingly. The dashed lines represent the locations of the separatrix.

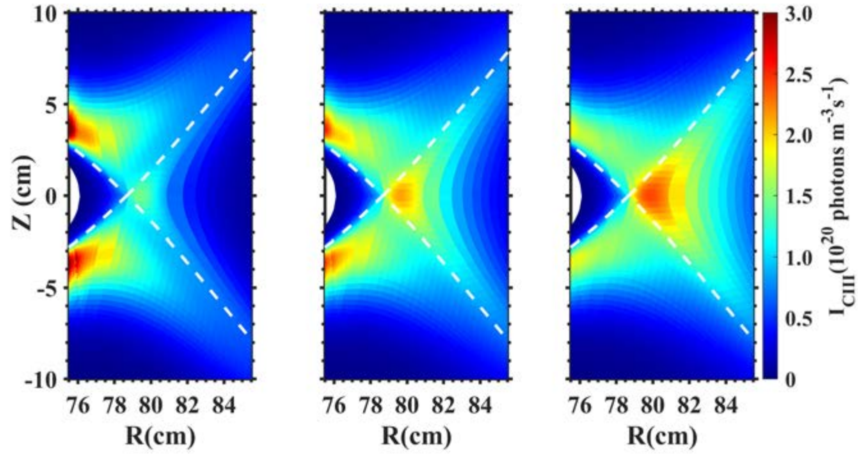

Figure 16. 2D CIII radiation intensity distributions for $D_{\perp,\mathrm{imp}} = 2\ \mathrm{m^2s^{-1}}$, $5\ \mathrm{m^2s^{-1}}, 10\ \mathrm{m^2s^{-1}}$ with $I_{\mathrm{div}} = 15$ kA. The dashed lines represent the locations of the separatrix.

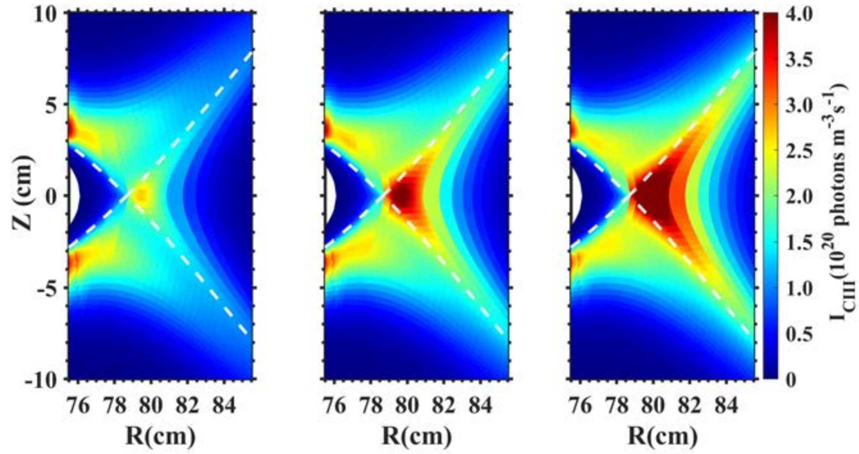

Figure 17. 2D CIII radiation intensity distributions for $E_{0,\mathrm{imp}} = 0.5$ eV, 1 eV, 1.5 eV with $I_{\mathrm{div}} = 15$ kA. The dashed lines represent the locations of the separatrix.

In J-TEXT divertor configuration, the location of X-point influences the magnetic field structures, the magnetic field line connection length in the SOL. The distribution of the main plasma changes with the magnetic field. The impurity source flux, the sputtering initial energy and the impurity exhaust are modified by the change of the magnetic field and the main plasma. So that the penetration depth of the impurity changes with the X-point location. Aiming to explore the influences of the X-point position on the SOL plasma transport, an I_{div}-scan is performed, otherwise based on the same input parameters as defined for the $I_{\mathrm{div}} = 12\ \mathrm{kA}$ case in table 3. Figure 18 shows the simulated particle- and power-fluxes on the high-field side target with $I_{\mathrm{div}} = 15\ \mathrm{kA}, 12\ \mathrm{kA}, 10\ \mathrm{kA}$. The divertor target power flux decay length (obtained by e-exponential fitting of the power flux distribution at the target according to the formula $q_{\|} = q_{\|,0}\mathrm{e}^{\frac{R-R_0}{\lambda_q}}$. $q_{\|,0}$ is the power flux at the separatrix. R_0 is the radial location of the separatrix. $q_{\|}$ is the power flux distribution with respect to the radial location R and the λ_q represents the power flux decay length.) is 3.3 cm, 3.8 cm, 4.6 cm (for $I_{\mathrm{div}} = 15\ \mathrm{kA}, 12\ \mathrm{kA}, 10\ \mathrm{kA}$ respectively). The corresponding power through target (proportion in P_{SOL}) is about 75 kW (69%), 71 kW (66%) and 58 kW (54%). The corresponding energy losses caused by the carbon radiation are 7.89 kW, 8.90 kW and 9.35 kW as shown in figure 19. As the X-point moves towards the target, the heat and particle fluxes on the divertor target become wider and wider, and their peaks decrease. Coupled linearly with the recycling flux, the resulting total carbon source flux is 27.56 A, 25.79 A and 23.80 A respectively, which means that the amount of sputtered carbon particles decreases when the X-point moves towards the target. However, the corresponding average carbon impurities density at the separatrix is $3.94\times10^{16}\ \mathrm{m}^{-3}$, $5.56\times10^{16}\ \mathrm{m}^{-3}$, $8.09\times10^{16}\ \mathrm{m}^{-3}$, respectively. With the X-point moving away from the target, more carbon impurities are sputtered, but the average carbon impurities density at the separatrix is lowered, indicating an enhanced SOL impurity screening effect. This result is consistent with the experimental finding in figure 8.

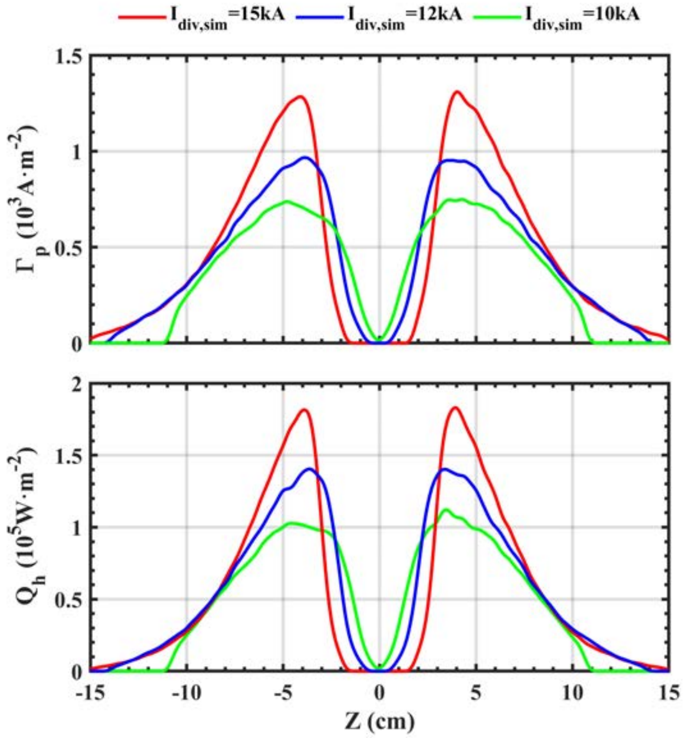

Figure 18. Simulated target particle flux and the simulated target heat flux (φ=0) with $I_{\rm div} = 15$ kA, 12 kA, 10 kA.

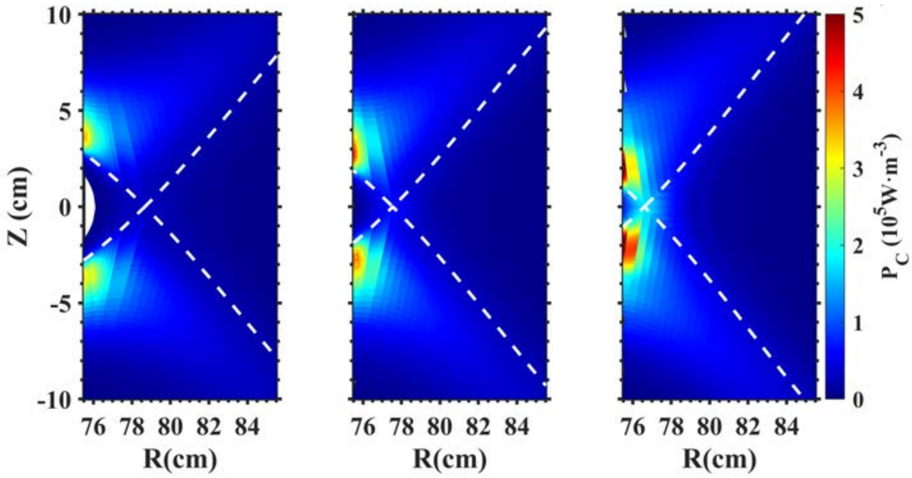

Figure 19. Simulated 2D carbon radiation density with $I_{\rm div} = 15$ kA, 12 kA, 10 kA with otherwise identical simulation parameters.

4. Conclusion and discussion

High-density experiments in a HFS single-null mid-plane divertor configuration on J-TEXT have been carried out to explore the influence of the X-point location and the density ramp-up on the SOL plasma transport. The experiment results show that the divertor configuration increases the maximum electron density before disruption and the Greenwald fraction. Moving the X-point away from the target was shown to improve both the plasma- and impurity-transport. With increasing the plasma density, the SOL electron temperature dropped, and the target ion saturation flux increased faster than the ion saturation flux measured by the reciprocating probe, which may result from the radial transport changes with the density ramp-up. Meanwhile, the impurity radiation was enhanced, which is helpful to reduce the target heat load. Under Ohmic discharge conditions, the core radiation is dominant, and the ratio of the downstream flux to the upstream flux is still linear as the plasma density rises. Limited by the open divertor without the neutralized gas pumping system and the low heating power, no high recycling regime was observed in this experiment.

EMC3-EIRENE was applied to study the SOL plasma transport in HFS mid-plane single-null configurations on J-TEXT. Good qualitative agreements between simulation results and the RP diagnostic results are obtained. The simulation results provided detailed 2D distributions of the main plasma parameters. When the X-point moves away from the target, simulations show an enhanced impurity screening, which is helpful to reduce the carbon impurity concentration in the core region.

Combined with the experiments and simulation results, with the change of the X-point location, the magnetic field structures and the connection length of magnetic field lines are modified in the SOL. The distributions of the main plasma and the impurity in the SOL change with the magnetic field. Besides, with the distance between the X-point and the divertor target increasing, the peak of the divertor heat flux increases and the divertor heat flux decay length decreases.

Even though simulation results are consistent with the RP diagnostic results, there are still some discrepancies between the simulations and the Doppler CIS diagnostic results. The possible explanation is the underestimate of the impurity cross-field coefficient and the impurity sputtering initial energy. Another explanation might be the presence of other impurities in the plasma, which increase the temperature gradient between the upstream plasma and the downstream plasma in the SOL. The application of EMC3-EIRENE on J-TEXT needs further optimization to introduce more impurity species, which may have significant influence on the plasma in experiments. Besides, based on the more detailed diagnostics, the optimizations of the parameters including $E_{0,\mathrm{imp}}$ and $D_{\perp,\mathrm{imp}}$ may contribute to offset the discrepencies between the simulaitons and experiments. The radial distributions of the electron density and temperature were measured by the RP. More stable plasma position- and density-control would make the measurements more accurate and improve the accuracy of the simulation parameters. Additionally, the application of non-uniform transport coefficients may yield a meaningful approach for further optimizing future studies. Furthermore, in future experiments, the introduction of ECRH, which has been working well on J-TEXT, could help to further increase the edge plasma density and improve the edge plasma and impurity transport. This might enable the device to explore higher plasma density ranges, which would be of interest also for HFS divertor studies.

Acknowledgments

This work is supported by the National Magnetic Confinement Fusion Energy R&D Program of China (No. 2018YFE0301104 and No. 2018YFE0309100), and National Natural Science Foundation of China (No. 51821005).

References

[1] Pitcher C S, Stangeby P C 1997 *Plasma Phys. Control. Fusion* **39** 779
[2] Guo H Y *et al* 2019 *Nucl. Fusion* **59** 086054
[3] Ryutov D D and Soukhanovskii V A 2015 *Phys. Plasmas* **22** 110901
[4] Ohyabu N *et al* 1994 *Nucl. Fusion* **34** 387
[5] Strumberger E 1996 *Nucl. Fusion* **36** 891
[6] Kukushkin A S *et al* 2011 *Fusion Eng. Des.* **86** 2865
[7] Stangeby P C 2000 *The Plasma Boundary of Magnetic Fusion Devices* (Boca Raton: CRC Press)
[8] Lackner K and Keilhacker M 1984 *J. Nucl. Mater.* **128-129** 368
[9] Wischmeier M *et al* 2009 *J. Nucl. Mater.* **390-391** 250
[10] Matthews G F 1995 *J. Nucl. Mater.* **220-222** 104
[11] Zhang M *et al* 2015 *J. Fusion Energy* **34** 509
[12] Liang Y *et al* 2019 *Nucl. Fusion* **59** 112016
[13] Chen Z P Realization of divertor configuration discharge in J-TEXT tokamak In: *Proceeding of the 28th IAEA Fusion Energy Conference* Vienna: IAEA 2021
[14] Feng Y *et al* 1997 *J. Nucl. Mater.* **241-243** 930
[15] Feng Y *et al* 2004 *Contrib. Plasma Phys.* **44** 57
[16] Feng Y *et al* 2013 *Comput. Phys. Commun.* **184** 1555
[17] Kobayashi M *et al* 2014 *Contrib. Plasma Phys.* **54** 383
[18] Feng Y *et al* 2014 *Contrib. Plasma Phys.* **54** 426
[19] Schneider R *et al* 1992 *J. Nucl. Mater.* **196** 810
[20] Reiter D, Baelmans M and Börner P 2005 *Fusion Sci. Technol.* **47** 172
[21] Zhang X L *et al* 2014 *Rev. Sci. Instrum.* **85** 11E420
[22] Li J C *et al* 2014 *Rev. Sci. Instrum.* **85** 11E414
[23] Chen J *et al* 2012 *Rev. Sci. Instrum.* **83** 10E306
[24] Long T *et al* 2020 *Rev. Sci. Instrum.* **91** 083504
[25] Lao L L *et al* 1985 *Nucl. Fusion* **25** 1611
[26] Greenwald M *et al* 1988 *Nucl. Fusion* **28** 2199
[27] Effenberg F *et al* 2017 *Nucl. Fusion* **57** 036021
[28] Kawamura G *et al* 2014 *Contrib. Plasma Phys.* **54** 437
[29] Kawamura G *et al* 2018 *Plasma Phys. Control. Fusion* **60** 084005
[30] Dai S Y *et al* 2018 *Nucl. Fusion* **58** 096024

[31] Oishi T *et al* 2018 *Nucl. Fusion* **58** 016040
[32] Dai S Y *et al* 2016 *Nucl. Fusion* **56** 066005
[33] Kobayash M *et al* 2004 *Contrib. Plasma Phys.* **44** 25
[34] Frerichs H *et al* 2010 *Nucl. Fusion* **50** 034004
[35] Lunt T *et al* 2012 *Nucl. Fusion* **52** 054013
[36] Harting D *et al* 2011 *J. Nucl. Mater.* **415** S540
[37] Lunt T *et al* 2014 *Plasma Phys. Control. Fusion* **56** 035009
[38] Huang J *et al* 2014 *Plasma Phys. Control. Fusion* **56** 075023
[39] Dai S Y *et al* 2021 *Plasma Phys. Control. Fusion* **63** 025003
[40] Dai S Y *et al* 2020 *J. Plasma Phys.* **86** 815860303
[41] Liu B *et al* 2020 *Plasma Phys. Control. Fusion* **62** 035003
[42] Xie T *et al* 2018 *Nucl. Fusion* **58** 106017
[43] Xu S *et al* 2018 *Nucl. Fusion* **58** 106008
[44] Xu S *et al* 2020 *Nucl. Fusion* **60** 056006
[45] https://www.adas.ac.uk
[46] Liang Z *et al* 2021 *Phys. Scr.* **96** 065601
[47] Feng Y *et al* 2009 *Nucl. Fusion* **49** 095002
[48] Zhao Q *et al* 2021 *IEEE 4th International Electrical and Energy Conference* DOI: 10.1109/CIEEC50170.2021.9510443